Modulation of polaritons in chemically doped graphene ribbon/α-MoO_3 heterostructures†

Min Liu,‡[a,b] Zhuoxin Xue,‡[b,c] Chengyu Jiang,[b,c] Hualong Zhu,[b,c] Shenghan Zhou,[d] Yuchuan Xiao,[e] Xian Wang,[f] Xiaoqing Xi,[f] Hanchao Teng,*[b,c] Na Chen*[b,c] and Hai Hu *[b,c]

Optical modulation is fundamental to photonics and optoelectronics, yet conventional modulators are often constrained by their physical size and operational efficiency. Two-dimensional (2D) materials, owing to their exceptional properties, offer compelling prospects for developing compact and efficient optical modulators. This study introduces a nanoscale polariton phase modulator utilizing a graphene/α-MoO_3 van der Waals heterostructure. By hybridizing surface plasmon polaritons in graphene with phonon polaritons in α-MoO_3, we realize a hybridized plasmon–phonon polariton (HPPP) mode. Chemical doping is employed to modulate the carrier concentration in graphene, which in turn induces a continuous topological transformation of the HPPP isofrequency contours in momentum space from hyperbolic to elliptical. This transformation directly alters the HPPP transmission wave vectors, enabling effective phase modulation within the heterostructure. Scanning near-field optical microscopy measurements reveal that the phase shift of the HPPP mode can be precisely controlled from 0 to π by varying the Fermi energy of graphene between 0.2 and 0.7 eV. Furthermore, the phase modulation effect is frequency-dependent, exhibiting robust controllability across the lower Reststrahlen band of α-MoO_3. This HPPP modulation scheme based on the graphene/α-MoO_3 heterostructure presents a novel technological pathway for creating ultra-compact optical modulators, holding significant potential for subwavelength-scale optical manipulation.

Introduction

Optical modulation is a cornerstone of modern photonics and optoelectronics, underpinning diverse applications such as wavefront manipulation,[1] optical signal processing,[2] phased arrays,[3] modulators,[4] and sensors.[5] While mature platforms—such as silicon photonics,[6] lithium niobate,[7] III–V semiconductors,[8] and plasmonic waveguides[9]—have advanced the field, the integration of optical and electronic components is still fundamentally constrained by the diffraction limit.[10] Conventional modulators, often spanning hundreds of microns to millimeters, are considerably larger than nanoscale electronic devices. This pronounced size mismatch highlights the pressing need for miniaturized modulators that offer compactness, high efficiency, and low power consumption, thereby paving the way for next-generation optoelectronic integration.

Polaritons, which are hybrid light–matter quasiparticles, facilitate light confinement far below the diffraction limit,[11,12] presenting a promising avenue for nanoscale optical control. Among various polaritonic systems, two-dimensional (2D) materials are particularly appealing due to their atomic-scale thickness,[13] tunable band structures,[14] and compatibility with van der Waals heterostructures.[15,16] These attributes result in polaritons characterized by strong field confinement, broad bandwidth,[17] long propagation lengths,[18] and the potential for electrical control,[19] rendering them exceptional candidates for nanophotonic integration.[20–22]

In such platforms, graphene/α-MoO_3 heterostructures offer distinct advantages stemming from their distinctive coupling characteristics. Graphene hosts broadband, tunable surface

[a]Henan Institute of Advanced Technology, Zhengzhou University, Zhengzhou 450001, China
[b]CAS Key Laboratory of Nanophotonic Materials and Devices, CAS Key Laboratory of Standardization and Measurement for Nanotechnology, National Center for Nanoscience and Technology, Beijing 100190, P. R. China.
E-mail: tenghc2019@nanoctr.cn, chenn2019@nanoctr.cn, huh@nanoctr.cn
[c]Center of Materials Science and Optoelectronics Engineering, University of Chinese Academy of Sciences, Beijing 100049, P. R. China
[d]School of Materials Science and Engineering, Shanghai Jiao Tong University, Shanghai, 200240, China
[e]Suzhou Laboratory, Suzhou, 215100, China
[f]State Key Laboratory of New Ceramic Materials & Fine Processing, Tsinghua University, Beijing 100084, P. R. China
†Electronic supplementary information (ESI) available. See DOI: https://doi.org/10.1039/d5nr01014d
‡These authors contributed equally.

plasmon polaritons (SPPs),[23] whereas α-MoO_3, a naturally hyperbolic and anisotropic van der Waals crystal, supports low-loss, directionally propagating phonon polaritons (PhPs).[24] The synergistic coupling between these materials gives rise to the formation of hybrid plasmon–phonon polaritons (HPPPs) endowed with high tunability, long propagation distance, strong anisotropy, and controllable dispersion topology,[25–29] thereby providing an excellent platform for polariton modulation. However, the development of nanoscale phase modulators based on topological transitions of these HPPPs has remained largely unexplored.

Building upon this foundation, we demonstrate a nanoscale polariton phase modulator using a graphene/α-MoO_3 heterostructure. This device enables active and broadband phase control by manipulating the topological transitions of HPPPs, achieved through chemical tuning of graphene Fermi energy. Specifically, by adjusting the graphene Fermi energy from 0.2 to 0.7 eV, we induce a continuous transformation of the HPPP isofrequency contours from hyperbolic to the elliptical shape. This transformation enables precise tuning of the transmission wave vector and the effective phase of PhPs in the heterostructure. Scanning near-field optical microscopy (s-SNOM) measurements validate these findings, revealing a continuous HPPP phase shift from 0 to π, with robust controllability across the lower Reststrahlen band of α-MoO_3. This work establishes a new platform for ultra-compact, tunable optical modulators with strong potential for subwavelength optical signal processing.

Results and discussion

Fig. 1(a) illustrates the proposed structure, which features a 260 nm thick α-MoO_3 layer transferred on a gold substrate. A resonant Au antenna is fabricated on the α-MoO_3 surface to facilitate the excitation of polaritons. This study specifically investigates the phenomena within Reststrahlen band II of α-MoO_3, covering the frequency range of 816–976 cm^{-1}. In this spectral region, the dielectric tensor components of natural α-MoO_3 satisfy the conditions $\varepsilon_x < 0$, $\varepsilon_y > 0$, and $\varepsilon_z > 0$, which underpin the in-plane hyperbolic behavior of the phonon polaritons (PhPs).[30,31] To achieve phase modulation, a graphene ribbon, fabricated by electron beam lithography, is aligned along the *y*-direction ([001] crystal direction) within the α-MoO_3 layer, serving as the modulation region. In this graphene/α-MoO_3 heterostructure, surface plasmon polaritons (SPPs) in graphene couple with the PhPs in α-MoO_3, forming a hybrid plasmon–phonon polariton mode. Since the SPPs in graphene are highly sensitive to the Fermi energy, the HPPPs can be dynamically tuned by adjusting the carrier concentration in the monolayer graphene ribbon, allowing precise control over the transmission phase. Fig. 1(b and c) show simulated electric field distributions for graphene Fermi energy of 0 eV and 0.7 eV, respectively. As the polaritons propagate through the graphene/α-MoO_3 heterostructure modulation region, a significant phase shift in the HPPP mode is observed. This phase modulation is further confirmed by the third-order near-field optical measurements (S_3) shown in

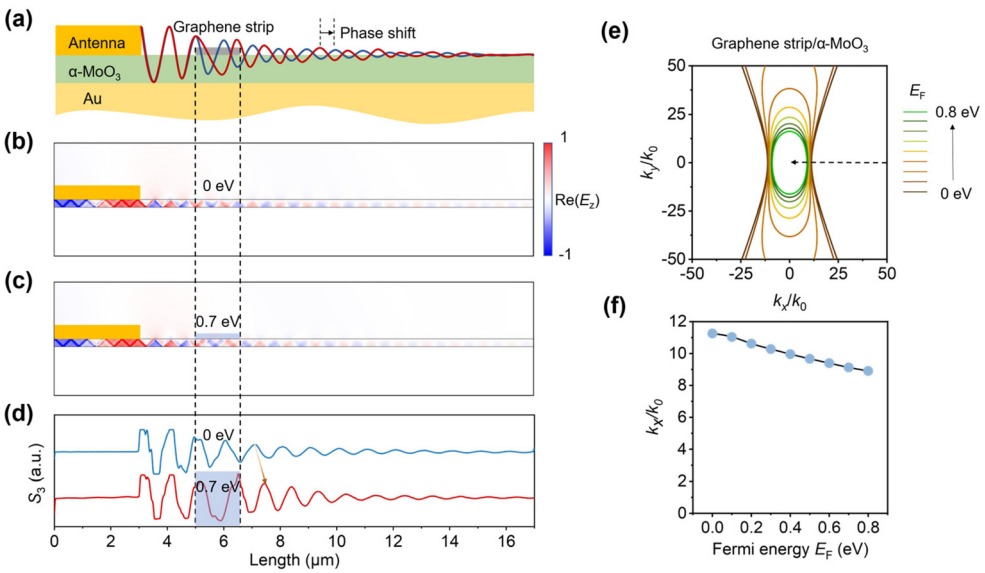

Fig. 1 Polariton phase modulation based on the graphene/α-MoO_3 heterostructure. (a) Schematic illustration of the graphene/α-MoO_3 structure. An Au antenna is on the surface to excite polaritons. (b and c) Electric field intensity distribution along the *x*-axis (E_z) at an incident light frequency of 893 cm^{-1}, with graphene Fermi energies of 0 eV and 0.7 eV, respectively. (d) The corresponding simulated near-field third-order optical signal along the *x*-axis at 893 cm^{-1}, with Fermi energies of 0 eV and 0.7 eV, respectively. (e) Calculated HPPP isofrequency contours for the graphene/α-MoO_3 heterostructure on the Au substrate at 893 cm^{-1}. Here, k_x and k_y represent the wave vectors of the polariton along the *x* ([100]) and *y* ([001]) crystal directions of α-MoO_3, respectively, and k_0 is the wave vector of light in free space. (f) Ratio of the polariton wave vector along the *x* direction of α-MoO_3 to the incident light wave vector.

Fig. 1(d). After traversing a 1.5 μm long modulation region, the PhP phase experiences a delay of approximately 0.6π.

To further elucidate the dynamic control mechanism of the in-plane HPPP dispersion contour topology in the graphene/α-MoO_3 heterostructure, we present the isofrequency dispersion contours (IFCs) for different graphene Fermi energies at a fixed incident wavelength of λ_0 = 11.20 μm (893 cm^{-1}), as shown in Fig. 1(e). The calculation method is detailed in the Methods section. In the absence of graphene, the in-plane PhPs in α-MoO_3 exhibit hyperbolic IFCs, indicating the absence of propagation modes along the *y*-axis ([001] crystal direction). At lower graphene Fermi energies, the HPPP in the graphene/α-MoO_3 heterostructure is primarily governed by the PhPs of α-MoO_3, with the IFCs retaining a hyperbolic morphology. As the graphene Fermi energy increases to 0.7 eV, the HPPPs transition from being PhP dominated to SPP dominated. Concomitantly, as the dielectric environment is altered by the changing graphene Fermi energy, the SPP wavelength shifts. This shift causes the opening angle of the hyperbolic IFCs to gradually expand, culminating in a topological transition from an open (hyperbolic) to a closed (elliptical) geometry.

Additionally, we analyze the variation trend of the HPPP wavelength compression ratio k_x/k_0 along the propagation direction in α-MoO_3 (*x*-direction), as shown in Fig. 1(f). As the Fermi energy is elevated, graphene SPPs increasingly dominate the HPPP characteristics in the graphene/α-MoO_3 heterostructure. Consequently, the wavefront becomes more sensitive to Fermi energy variations. Moreover, with increasing graphene Fermi energies, the k_x/k_0 of the HPPP exhibits a monotonic decline, indicating progressive elongation of polariton wavelengths.[25] This phenomenon provides an additional degree of freedom for dynamically controlling the polariton propagation and phase.

To validate the phase modulation effect, we designed and fabricated the corresponding heterostructure, as illustrated in the schematic of Fig. 2(a). The propagation of polaritons within the graphene/α-MoO_3 heterostructure was directly observed using scanning near-field optical microscopy (s-SNOM). Under p-polarized infrared illumination, nanoscale localized fields generated at both ends of the resonant gold antenna efficiently excite the HPPP mode. This excitation produces detectable polariton wavefronts within the modulation region. During s-SNOM sample scanning, both the real part of the scattered electric field and the surface morphology were simultaneously recorded, enabling direct measurement of the vertical near-field component of the HPPP wavefront excited by the gold antenna. Fig. 2(b) displays the optical microscopy image of the fabricated sample, with additional details available in ESI Fig. S1.† Moreover, the AFM image obtained *via* s-SNOM, shown in Fig. 2(c), confirms the height uniformity and surface cleanliness of the graphene ribbon. This demonstrates superior sample quality for the ensuing experimental analysis.

Using chemical vapor doping for Fermi-level engineering in graphene, we systematically investigated hyperbolic plasmon-polaritons in the heterostructure across a tunable Fermi energy range of E_F = 0.2–0.7 eV. This investigation was conducted using scattering-type near-field optical microscopy (s-SNOM). As depicted in Fig. 2(d)–(f) (with the complete dataset in ESI Fig. S2†), the real-space nanoimaging reveals that polariton propagation characteristics are modulated by doping, governed by variations in carrier density. The experimental results indicate that at low doping levels (E_F = 0.2 eV), the phase modulation effect is less pronounced. At this low Fermi energy, the HPPP is predominantly governed by the PhPs of α-MoO_3, exhibiting a hyperbolic wavefront with negligible influence from the surrounding dielectric environment.

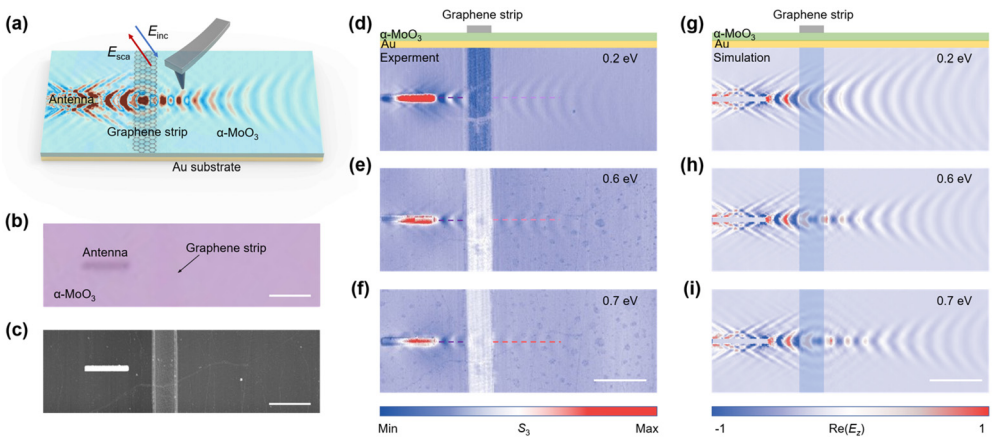

Fig. 2 Near-field optical imaging of polariton phase modulation in the graphene/α-MoO_3 heterostructure. (a) Schematic illustration of the phase modulation principle, demonstrating a significant phase shift in the polariton after passing through the modulation region. E_{inc} and E_{sca} represent the incident and scattering electromagnetic waves, respectively. (b and c) Optical microscopy and atomic force microscopy (AFM) images of the device, composed of a gold antenna, thin-layer α-MoO_3, and monolayer graphene, with a scale bar of 3 μm. (d–f) Experimentally measured near-field third-order optical signals along the *x*-direction at graphene Fermi energies of 0.2 eV, 0.6 eV, and 0.7 eV, respectively. (g–i) The corresponding numerically simulated electric field intensity distribution (E_z). The white scale bar corresponds to 3 μm.

When the Fermi energy of graphene increases to 0.6 eV, the HPPP in the graphene/α-MoO_3 modulation region becomes dominated by the SPPs of graphene. This results in progressively more developed elliptical wavefront features. Under these conditions, the phase of the polaritons undergoes a significant shift after passing through the graphene/α-MoO_3 modulation region. Upon further increasing the Fermi energy to 0.7 eV, the elliptical wavefront of the HPPP becomes even more pronounced, the wavelength increases, and the phase modulation effect is consequently enhanced. Fig. 2(g–i) display the simulated near-field mode images corresponding to these experimental results, which closely match the experimental observations, thereby validating the reliability of our experimental methodology. It is important to note that the phase modulation arises from the tuning of the Fermi energy of graphene within the graphene/α-MoO_3 heterostructure, rather than from the α-MoO_3 flake alone (ESI Fig. S3†).

From the experimental and simulated images in Fig. 2(d–i), we quantitatively extracted the third-order near-field signal (S_3) of the PhPs in graphene/α-MoO_3 heterostructures, comparing unmodulated regions (dark-purple dashed contours) with modulated zones (light-purple, pink, and red dashed contours). Detailed analysis protocols are provided in ESI Fig. S4.† Crucially, systematic Fermi energy tuning of graphene demonstrates a negligible impact on the intrinsic PhP wavelength within α-MoO_3 unmodulated areas, establishing these regions as phase reference benchmarks. This calibration enables the precise determination of active modulation-induced phase shifts, which are graphically represented by vertical dashed guide lines in Fig. 3(a). As shown in Fig. 3(a), the modulated phase difference modulation exhibits a proportional increase with the increase in the graphene Fermi energy. To explain this phenomenon, we propose a simple optical path length model to describe the phase modulation mechanism of the graphene/α-MoO_3 heterostructure. This model provides theoretical guidance for designing such phase modulators. The phase shifts for different Fermi energies are shown in Fig. 3(b). For PhPs propagating through the graphene/α-MoO_3 modulation region, the phase shift can be expressed as:

$$\Delta\varphi = 2\pi \int_0^{L_0} \frac{n - n_0}{\lambda_0} \mathrm{d}L \tag{1}$$

where L_0 denotes the length of the graphene/α-MoO_3 modulation region; λ_0 and n_0 represent the wavelength and refractive index of the PhPs in the reference region without graphene, respectively; and n is the refractive index in the graphene/α-MoO_3 modulation region, which can be calculated using $n = k_x/k_0$. Therefore, by varying the graphene Fermi energy (*i.e.*, its doping level) to control the wave vector, the refractive index can be changed. Based on existing research, common methods for doping the graphene Fermi energy include electrical doping, van der Waals heterostructure doping, and chemical doping. Electrical doping[19] enables dynamic control but typically struggles to achieve high doping levels, while van der Waals heterostructure doping[32,33] often lacks *in situ* tunability. Consequently, we adopt chemical doping with NO_2,[34] where the doping status variation enables dynamic modification of the graphene Fermi energy.

Using eqn (1), we calculated the refractive index variation within the graphene/α-MoO_3 modulation region as a function of the Fermi energy. This calculation was based on phase difference results from both experiments and simulations, conducted at a fixed incident light frequency of 893 cm^{-1}. The results of this calculation are shown in Fig. 3(c) which reveals the refractive index shift. As graphene Fermi energy increases, the refractive index gradually reduces. This reduction leads to a shortened optical path length, consequently inducing the observed phase difference shifts. While this indicates a positive correlation between increasing Fermi energy and increasing phase shift (due to decreasing refractive index), the relationship is not strictly linear. Instead, it originates from

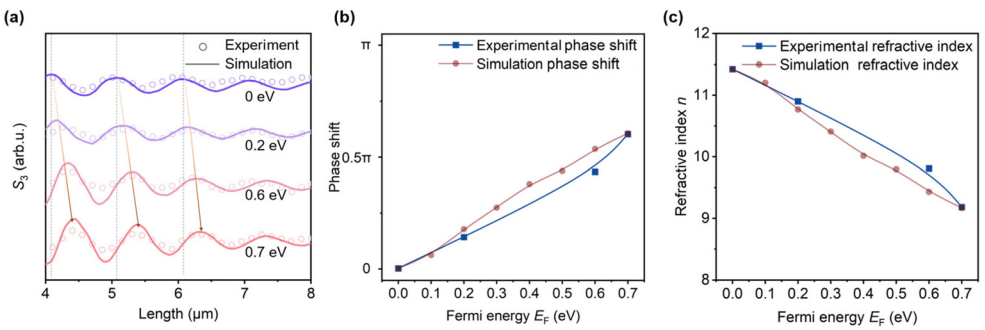

Fig. 3 Polariton phase shift and effective refractive index analysis based on the graphene/α-MoO_3 heterostructure. (a) Experimental near-field third-order optical signal (S_3) profiles of polaritons along the *x*-direction. These profiles are extracted along the central horizontal dashed lines indicated in the experimental images of Fig. 2(d–f) for different graphene Fermi energies. The vertical dashed lines in this panel serve as visual guides, with the set of lines for the E_F = 0 eV case (representing the reference or unmodulated region) illustrating a characteristic polariton wavelength for comparison. All experimental results were obtained from *in situ* samples. (b) Polariton phase shift plotted against graphene Fermi energy. This panel includes both experimental data (blue squares), extracted from the measurements shown in Fig. 2(d–f), and simulated data (red circles), derived from simulations corresponding to Fig. 2(g–i). (c) Effective refractive index (*n*) within the graphene/α-MoO_3 heterostructure modulation region as a function of graphene Fermi energy. Both experimental (blue squares) and simulated (red circles) values are presented.

the more intricate coupling between graphene and α-MoO_3.[25–29] The experimentally observed trend of refractive index variation observed in experiments is consistent with the trend of k_x/k_0 (Fig. 1(f)). This consistency provides intuitive evidence supporting the proposed modulation mechanism.

It is worth emphasizing that the optical path is defined by $L = nL_0$. Thus, for a fixed refractive index, the optical path length inherently depends on the spatial length of the modulation region. Consequently, increasing the width of the graphene ribbon leads to a proportional enhancement in the phase modulation efficacy, thereby enabling improved phase modulation amplitude for identical variations in the graphene Fermi energy. This fundamental relationship establishes a key design strategy for optimizing phase modulators based on graphene/α-MoO_3 heterostructures.

Given the strong frequency dependence of the relative permittivity of both α-MoO_3 and graphene, we systematically investigate the polaritonic phase shift after passing through the graphene/α-MoO_3 modulation region under varying excitation frequencies. Experiments are conducted at incident light frequencies of 900 cm^{-1} and 905 cm^{-1}. The corresponding experimental and simulated near-field optical images are provided in ESI Fig. S5.† The extracted experimental third-order electric field intensity for these frequencies is shown in Fig. 4(a) and (b). These results reveal that as the incident light frequency increases, the refractive index variation of the HPPP in the high-frequency range exhibits a substantially stronger dependence on the graphene Fermi energy. This, in turn, leads to an enhanced phase shift. This phenomenon underscores the frequency dependence of HPPP phase modulation, thereby enabling more flexible phase control by tuning the incident light frequency.

By leveraging the long lifetime of phonon polaritons in α-MoO_3 and the dynamic tunability of SPPs in graphene, we successfully achieve phase modulation of PhPs over a broad frequency range. This characteristic highlights the broadband spectral tunability of our proposed scheme, providing new possibilities for multi-band phase manipulation. Notably, the inherent challenge in directly controlling phonon polaritons necessitates obtaining substantially high Fermi energy in graphene to realize significant HPPP phase modulation. Future implementations could incorporate high-efficiency SPP modulation materials such as black phosphorus[35,36] to further enhance PhP manipulation capabilities. This strategy is anticipated to advance multi-dimensional subwavelength-scale sensing and on-chip optical manipulation, thereby presenting innovative approaches for the design of ultra-compact photonic devices.

Conclusions

In conclusion, this study presents and experimentally demonstrates a graphene/α-MoO_3 heterostructure-based scheme. This scheme leverages the hybridized coupling between surface plasmon polaritons (SPPs) in graphene and phonon polaritons (PhPs) in α-MoO_3 to form a distinctive hybrid plasmon–phonon polariton (HPPP) mode. By integrating the pronounced in-plane anisotropic propagation characteristics of PhPs in α-MoO_3 with the carrier density-dependent tunability of graphene's SPPs, this hybrid configuration enables effective *in situ* phase control of the HPPP. Through gas-doping-mediated adjustment of the carrier concentration in monolayer graphene, we have shown that the HPPP transmission mode undergoes a controllable topological transition between hyperbolic and elliptical dispersion regimes. This transition facilitates continuous phase modulation of the HPPP spanning the 0–π range. The proposed HPPP-based modulation principle is not limited to this specific system and can be extended to other Reststrahlen bands of α-MoO_3 and other two-dimensional (2D) materials, such as hexagonal boron nitride (*h*-BN). This work shows promising potential for the development of ultra-compact optical modulators,[37] biosensors,[34] and related applications, offering a new paradigm for creating high-efficiency integrated nanophotonic devices for subwavelength optical manipulation.

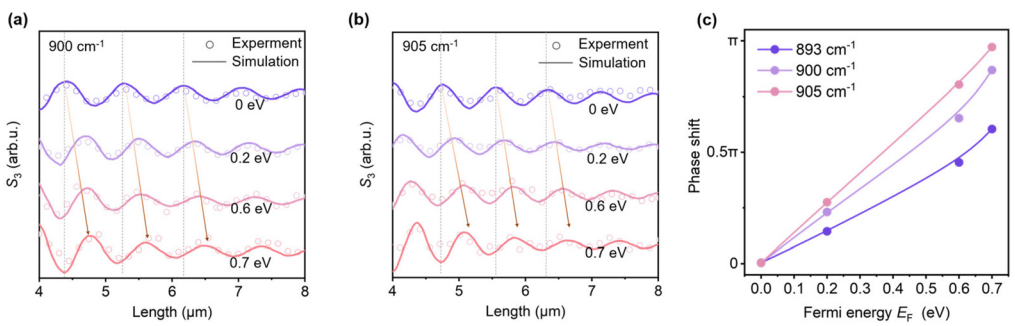

Fig. 4 Polariton phase shifts at different incident light frequencies. (a and b) Experimental (circles) and simulated (solid lines) near-field third-order optical signal (S_3) profiles of polaritons along the *x*-direction for incident light frequencies of 900 cm^{-1} (a) and 905 cm^{-1} (b), respectively. Each panel displays profiles for various graphene Fermi energies (E_F: 0 eV, 0.2 eV, 0.6 eV, and 0.7 eV), illustrating the phase shifts that are dependent on both incident frequency and E_F. (c) Extracted polariton phase shift as a function of graphene Fermi energy for three distinct incident light frequencies: 893 cm^{-1} (blue curve), 900 cm^{-1} (purple curve), and 905 cm^{-1} (pink curve).

Methods

Nanofabrication of the devices

In this study, high-quality α-MoO_3 flakes were exfoliated from bulk crystals grown *via* chemical vapor deposition (CVD) using mechanical exfoliation. These flakes were then precisely transferred onto a gold substrate using polydimethylsiloxane (PDMS) for deterministic dry transfer. Monolayer graphene was transferred using a polymethyl methacrylate (PMMA)-assisted method, where graphene was exfoliated from a CVD-grown graphene/copper foil structure and subsequently transferred onto the surface of α-MoO_3 flakes. The emission efficiency of the resonant antennas is primarily determined by the geometry, size, and frequency of the incident light. We designed gold antennas with a length of 3 μm and a thickness of 50 nm, optimized to efficiently excite polaritons within the frequency range of 890–950 cm^{-1}, corresponding to the Reststrahlen band II of α-MoO_3.

Electron beam lithography (Vistec 5000+ES) with a 100 kV beam was used to define the gold antenna array pattern in an approximately 350 nm thick PMMA950K resist deposited on the selected α-MoO_3 flakes. Subsequently, a titanium (Ti) adhesion layer (5 nm) and Au (50 nm) were deposited using electron beam evaporation in a vacuum chamber under pressure lower than 5×10^{-6} torr to fabricate the gold antennas. Electron beam evaporation was also employed to deposit approximately 60 nm of gold on a lightly doped silicon substrate, which served as the gold substrate. To remove any residual organic materials, the samples were immersed in a hot acetone bath at 80 °C for 25 minutes, followed by gentle rinsing with isopropyl alcohol for 3 minutes. The samples were then dried with nitrogen and baked in an oven.

The samples were annealed in a vacuum to remove most residual dopants introduced during the wet transfer process and then transferred to a chamber filled with NO_2 gas. Previous studies have shown that chemical doping enables reliable modulation of polariton properties, such as field confinement and in-plane wavelength.[38–41] Therefore, we adopt chemical doping with NO_2, where the doping status variation enables dynamic modification of the graphene Fermi energy. In the experiment, the samples are sealed in a chamber filled with N_2 containing 75% NO_2 gas for a period of time. The NO_2 molecules, acting as electron acceptors, are adsorbed onto the graphene surface, thereby inducing p-type doping. According to our previous experimental results, the Fermi energy of the doped graphene can be determined by analyzing the Raman spectra of G peak stiffening, 2D peak stiffening, or the intensity ratio $I_G//I_{2D}$.[23,25] Under a constant NO_2 gas concentration of 75%, the Fermi energy of graphene can be precisely controlled by adjusting the doping time. This chemical doping method offers excellent uniformity and stability, ensuring the accuracy of the measured Fermi energy values.[25] As demonstrated in our previous work, Raman mapping reveals the high uniformity of gas-doped graphene, while the Fermi level shows only a slight decrease from 0.7 to 0.6 eV after two weeks under ambient conditions, indicating excellent doping stability.[25] Moreover, the physical adsorption of NO_2 molecules enables reversible doping *via* vacuum annealing and re-doping.

Scanning near-field optical microscopy measurements

Optical near-field imaging was conducted using a scattering-type scanning near-field optical microscope (s-SNOM, Neaspec) equipped with a tunable quantum cascade laser (890–2000 cm^{-1}). The atomic force microscopy (AFM) tip, coated with gold, had a radius of approximately 25 nm (NanoWorld), with the tapping frequency and amplitude set to around 270 kHz and 30–50 nm, respectively. The laser beam was directed onto the AFM tip, with the lateral light spot size beneath the tip being approximately 25 μm, large enough to cover both the antenna and the graphene/α-MoO_3 sample. Third-order harmonic demodulation was applied to the near-field amplitude images for effective background noise suppression. In our experiments, p-polarized plane waves were incident at 60° relative to the tip axis. To eliminate effects caused by the optical anisotropy of α-MoO_3 due to the polarization direction relative to the crystal orientation, the in-plane projection of the polariton vector was aligned with the *x*-direction of α-MoO_3 ([100] crystal direction).

Calculation of polariton dispersion and IFCs of hybrid plasmon–phonon polaritons

The transfer matrix method is employed to analyze the dispersion characteristics and IFCs of hybrid plasmon–phonon polaritons in graphene-α-MoO_3 heterostructures. Our theoretical framework considers a three-layer structure: the first layer ($z > 0$, air) serves as the cover medium; the second layer ($0 > z > -d_h$, graphene/α-MoO_3) functions as the intermediate region; and the third layer ($z < -d_h$, Au) represents the substrate. Each layer is treated as a homogeneous material characterized by its respective dielectric tensor. The air and the substrate layers are modeled and described using tensors diag$\{\varepsilon_{a,s}\}$.[42] The α-MoO_3 film, in contrast, is modeled by an anisotropic diagonal tensor diag$\{\varepsilon_x, \varepsilon_y, \varepsilon_z\}$, where ε_x, ε_y, and ε_z correspond to the permittivity components along the *x*, *y*, and *z* axes, respectively. Additionally, monolayer graphene, positioned atop α-MoO_3 at $z = 0$, is represented as an infinitesimally thin current layer characterized by a frequency-dependent surface conductivity derived from the local random-phase approximation model:[43,44]

$$\sigma(\omega) = \frac{ie^2 k_B T\left(\omega + \frac{1}{\tau}\right)}{\pi\hbar^2}\left[\frac{E_F}{k_B T} + 2\ln\left(e^{-\frac{E_F}{k_B T}} + 1\right)\right] + i\frac{e^2}{4\pi\hbar}\ln\left[\frac{2|E_F| - \hbar\left(\omega + \frac{i}{\tau}\right)}{2|E_F| + \hbar\left(\omega + \frac{i}{\tau}\right)}\right] \quad \text{(S1)}$$

which is influenced by the Fermi energy E_F, the inelastic relaxation time τ and the temperature *T*; the relaxation time is expressed in terms of the graphene Fermi velocity $v_F = c/300$ and the carrier mobility μ, with $\tau = \mu E_F/ev_F^2$, where *e* is the

elementary charge; k_B is the Boltzmann constant; $\hbar$ is the reduced Planck constant; and ω is the illumination frequency.

Given the strong field confinement produced by the structure under consideration, only transverse magnetic (TM) modes are considered, as transverse electric (TE) components contribute negligibly. The corresponding p-polarization Fresnel reflection coefficient r_p of the three-layer system follows the analytical expression:

$$r_p = \frac{r_{12} + r_{23}(1 - r_{12} - r_{21})e^{i2k_z^{(2)}d_h}}{1 + r_{12}r_{23}e^{i2k_z^{(2)}d_h}}, \quad \text{(S2)}$$

$$r_{12} = \frac{Q_1 - Q_2 + SQ_1Q_2}{Q_1 + Q_2 + SQ_1Q_2}, \quad \text{(S3)}$$

$$r_{21} = \frac{Q_2 - Q_1 + SQ_1Q_2}{Q_2 + Q_1 + SQ_1Q_2}, \quad \text{(S4)}$$

$$r_{23} = \frac{Q_2 - Q_3}{Q_2 + Q_3}, \quad \text{(S5)}$$

$$Q_j = \frac{k_z^{(j)}}{\varepsilon_t^{(j)}}, \quad \text{(S6)}$$

$$S = \frac{\sigma Z_0}{\omega}. \quad \text{(S7)}$$

Here, r_{jk} refers to the reflection coefficient at the interface between media j and k (for j, k = 1, 2, 3), while $\varepsilon_t^{(j)}$ represents the in-plane dielectric function for a propagation wave vector $k_p(\theta)$ (with θ being the angle relative to the x-axis), which can be expressed as $\varepsilon_t^{(j)} = \varepsilon_x^{(j)}\cos^2\theta + \varepsilon_y^{(j)}\sin^2\theta$, in terms of $\varepsilon_x^{(j)}$ and $\varepsilon_y^{(j)}$ (*i.e.*, the diagonal dielectric tensor components of layer j along the x and y axes, respectively); $k_z^{(j)} = \sqrt{\varepsilon_t^{(j)}\frac{\omega^2}{c^2} - \frac{\varepsilon_t^{(j)}}{\varepsilon_z^{(j)}}q^2}$ is the out-of-plane wave vector, with $\varepsilon_z^{(j)}$ being the dielectric function of layer j along the z-axis and Z_0 the vacuum impedance.

The dispersion relation $q(\omega, \theta)$ is determined from the zeros of the denominator of eqn (S2):

$$1 + r_{12}r_{23}e^{i2k_z^{(2)}d_h} = 0. \quad \text{(S8)}$$

For simplicity, we assume a system with small dissipation, so that the maxima of Im$\{r_p\}$ approximately solves the condition given by eqn (S8), and therefore, produces the sought-after dispersion relation $q(\omega, \theta)$.

Electromagnetic simulations

Numerical modeling was performed using COMSOL Multiphysics simulation software. To improve computational efficiency, we constructed a streamlined 2D geometric model through dimensional reduction of the original 3D heterostructure as depicted in Fig. 1(a). Scattering boundary conditions were applied, with α-MoO_3 placed on a gold substrate to enhance wavelength compression and minimize polariton propagation loss. A monolayer graphene ribbon was positioned on the α-MoO_3 surface as the modulation region. Permittivities of Au (wavelength-dependent) and α-MoO_3 (fitted by the Lorentz model) were obtained from the reference respectively.[45,46] The graphene thickness was set to 0.34 nm, and its conductivity was modeled using the local random phase approximation with transition boundary conditions applied. The carrier mobility in graphene was preset to 2000 $cm^2\ V^{-1}\ s^{-1}$. To efficiently couple the polaritons, gold antennas served as the excitation source. These antennas generated strong counter-phase near-fields at their two ends, providing high-momentum near-field components that matched the wave vector of the polaritons, thereby exciting the propagation modes of phonon polaritons in α-MoO_3.[47,48] All numerical implementations maintained strict geometric correspondence with experimental configurations to ensure consistency between theoretical predictions and experimental observations.

Author contributions

H. H., N. C., and H. T. conceived the idea. H. H. supervised the project. N. C. and M. L. prepared the samples and conducted the near-field measurements. Z. X. and H. T. developed the theoretical framework and performed the simulations. M. L., Z. X., C. J., H. Z., S. Z., Y. X., X. W., X. X., H. T., N. C., and H. H. contributed to the data analysis and discussion of the results. M. L., Z. X., N. C., and H. T. co-wrote the manuscript with input and feedback from H. H.

Conflicts of interest

The authors declare no competing interests.

Data availability

The data that support the findings of this study are available within the paper and the ESI.†

Acknowledgements

This work was financially supported by the National Natural Science Foundation of China (grant no. 52322209, 52172139, and 52350314 to H. H.), the Beijing Nova Program (grant no. 2022012 and 20240484600 to H. H.), the Youth Innovation Promotion Association of Chinese Academy of Sciences (grant no. 2022037 to H. H.), the China Postdoctoral Science Foundation (grant no. 2024M760685 to N. C.), and the Natural Science Foundation of Shanghai (grant no. 24ZR1440800 to S. Z.).

References

1 C. U. Hail, M. Foley, R. Sokhoyan, L. Michaeli and H. A. Atwater, High quality factor metasurfaces for two-dimensional wavefront manipulation, *Nat. Commun.*, 2023, **14**, 8476.

2 J. B. Pendry, D. Schurig and D. R. Smith, Controlling Electromagnetic Fields, *Science*, 2006, **312**, 1780–1782.

3 J. Sun, E. Timurdogan, A. Yaacobi, E. S. Hosseini and M. R. Watts, Large-scale nanophotonic phased array, *Nature*, 2013, **493**, 195–199.

4 N. Yu and F. Capasso, Flat optics with designer metasurfaces, *Nat. Mater.*, 2014, **13**, 139–150.

5 Q. Yang, *et al.*, All–Optical Modulation Photodetectors Based on the CdS/Graphene/Ge Sandwich Structures for Integrated Sensing–Computing, *Adv. Sci.*, 2025, 2413662, DOI: **10.1002/advs.202413662**.

6 S. Abel, *et al.*, Large Pockels effect in micro- and nanostructured barium titanate integrated on silicon, *Nat. Mater.*, 2019, **18**, 42–47.

7 C. Wang, *et al.*, Integrated lithium niobate electro-optic modulators operating at CMOS-compatible voltages, *Nature*, 2018, **562**, 101–104.

8 K. Vyas, *et al.*, Group III-V semiconductors as promising nonlinear integrated photonic platforms, *Adv. Phys.: X*, 2022, **7**, 2097020.

9 A. Melikyan, *et al.*, High-speed plasmonic phase modulators, *Nat. Photonics*, 2014, **8**, 229–233.

10 K. Liu, C. R. Ye, S. Khan and V. J. Sorger, Review and perspective on ultrafast wavelength-size electro-optic modulators: Review and perspective on ultrafast wavelength-size electro-optic modulators, *Laser Photonics Rev.*, 2015, **9**, 172–194.

11 D. N. Basov, M. M. Fogler and F. J. García de Abajo, Polaritons in van der Waals materials, *Science*, 2016, **354**, aag1992.

12 S. Dai, *et al.*, Tunable Phonon Polaritons in Atomically Thin van der Waals Crystals of Boron Nitride, *Science*, 2014, **343**, 1125–1129.

13 F. H. L. Koppens, D. E. Chang and F. J. García de Abajo, Graphene Plasmonics: A Platform for Strong Light–Matter Interactions, *Nano Lett.*, 2011, **11**, 3370–3377.

14 A. N. Grigorenko, M. Polini and K. S. Novoselov, Graphene plasmonics, *Nat. Photonics*, 2012, **6**, 749–758.

15 G. Hu, *et al.*, Topological polaritons and photonic magic angles in twisted α-MoO3 bilayers, *Nature*, 2020, **582**, 209–213.

16 S. Dai, *et al.*, Graphene on hexagonal boron nitride as a tunable hyperbolic metamaterial, *Nat. Nanotechnol.*, 2015, **10**, 682–686.

17 X. Yang, *et al.*, Nanomaterial-Based Plasmon-Enhanced Infrared Spectroscopy, *Adv. Mater.*, 2018, **30**, 1704896.

18 G. X. Ni, *et al.*, Fundamental limits to graphene plasmonics, *Nature*, 2018, **557**, 530–533.

19 Z. Fei, *et al.*, Gate-tuning of graphene plasmons revealed by infrared nano-imaging, *Nature*, 2012, **487**, 82–85.

20 A. Woessner, *et al.*, Electrical 2π phase control of infrared light in a 350 nm footprint using graphene plasmons, *Nat. Photonics*, 2017, **11**, 421–424.

21 M. Liu, *et al.*, A graphene-based broadband optical modulator, *Nature*, 2011, **474**, 64–67.

22 G. X. Ni, *et al.*, Ultrafast optical switching of infrared plasmon polaritons in high-mobility graphene, *Nat. Photonics*, 2016, **10**, 244–247.

23 H. Hu, *et al.*, Active control of micrometer plasmon propagation in suspended graphene, *Nat. Commun.*, 2022, **13**, 1465.

24 G. Álvarez-Pérez, *et al.*, Infrared Permittivity of the Biaxial van der Waals Semiconductor α-MoO_3 from Near- and Far-Field Correlative Studies, *Adv. Mater.*, 2020, **32**, 1908176.

25 H. Hu, *et al.*, Doping-driven topological polaritons in graphene/α-MoO3 heterostructures, *Nat. Nanotechnol.*, 2022, **17**, 940–946.

26 H. Hu, *et al.*, Gate-tunable negative refraction of mid-infrared polaritons, *Science*, 2023, **379**, 558–561.

27 Y. Zeng, *et al.*, Tailoring topological transitions of anisotropic polaritons by interface engineering in biaxial crystals, *Nano Lett.*, 2022, **22**, 4260–4268.

28 L. Zhou, *et al.*, Engineering shear polaritons in 2D twisted heterostructures, *Nat. Commun.*, 2025, **16**, 2953.

29 F. L. Ruta, *et al.*, Surface plasmons induce topological transition in graphene/α-MoO3 heterostructures, *Nat. Commun.*, 2022, **13**, 3719.

30 J. Duan, *et al.*, Enabling propagation of anisotropic polaritons along forbidden directions via a topological transition, *Sci. Adv.*, 2021, **7**, eabf2690.

31 Q. Zhang, *et al.*, Hybridized Hyperbolic Surface Phonon Polaritons at α-MoO_3 and Polar Dielectric Interfaces, *Nano Lett.*, 2021, **21**, 3112–3119.

32 D. J. Rizzo, *et al.*, Charge-Transfer Plasmon Polaritons at Graphene/α-RuCl3 Interfaces, *Nano Lett.*, 2020, **20**, 8438–8445.

33 D. J. Rizzo, *et al.*, Nanometer-Scale Lateral p–n Junctions in Graphene/α-$RuCl_3$ Heterostructures, *Nano Lett.*, 2022, **22**, 1946–1953.

34 H. Hu, *et al.*, Gas identification with graphene plasmons, *Nat. Commun.*, 2019, **10**, 1131.

35 I.-H. Lee, *et al.*, Anisotropic Acoustic Plasmons in Black Phosphorus, *ACS Photonics*, 2018, **5**, 2208–2216.

36 L. Zeng, *et al.*, Surface and interface control of black phosphorus, *Chem*, 2022, **8**, 632–662.

37 R. Yu, R. Alaee, R. W. Boyd and F. J. G. De Abajo, Ultrafast Topological Engineering in Metamaterials, *Phys. Rev. Lett.*, 2020, **125**, 037403.

38 J. Taboada-Gutiérrez, *et al.*, Broad spectral tuning of ultra-low-loss polaritons in a van der Waals crystal by intercalation, *Nat. Mater.*, 2020, **19**, 964–968.

39 Y. Wu, *et al.*, Chemical switching of low-loss phonon polaritons in α-MoO_3 by hydrogen intercalation, *Nat. Commun.*, 2020, **11**, 2646.

40 Z. Zheng, *et al.*, Chemically-doped graphene with improved surface plasmon characteristics: an optical near-field study, *Nanoscale*, 2016, **8**, 16621–16630.

41 Z. Zheng, *et al.*, Highly Confined and Tunable Hyperbolic Phonon Polaritons in van der Waals Semiconducting Transition Metal Oxides, *Adv. Mater.*, 2018, **30**, 1705318.

42 J. Kischkat, *et al.*, Mid-infrared optical properties of thin films of aluminum oxide, titanium dioxide, silicon dioxide, aluminum nitride, and silicon nitride, *Appl. Opt.*, 2012, **51**, 6789–6798.
43 B. Wunsch, T. Stauber, F. Sols and F. Guinea, Dynamical polarization of graphene at finite doping, *New J. Phys.*, 2006, **8**, 318.
44 A. Y. Nikitin, *et al.*, Real-space mapping of tailored sheet and edge plasmons in graphene nanoresonators, *Nat. Photonics*, 2016, **10**, 239–243.
45 Z. Zheng, *et al.*, A mid-infrared biaxial hyperbolic van der Waals crystal, *Sci. Adv.*, 2019, **5**, eaav8690.
46 S. Babar and J. H. Weaver, Optical constants of Cu, Ag, and Au revisited, *Appl. Opt.*, 2015, **54**, 477.
47 P. Alonso-González, *et al.*, Controlling graphene plasmons with resonant metal antennas and spatial conductivity patterns, *Science*, 2014, **344**, 1369–1373.
48 P. Pons-Valencia, *et al.*, Launching of hyperbolic phonon-polaritons in h-BN slabs by resonant metal plasmonic antennas, *Nat. Commun.*, 2019, **10**, 3242.